Maximum Thrust per Ampere of Linear Induction Machine Based on Finite-Set Model Predictive Direct Thrust Control

Wei Xu, *Senior Member, IEEE*, Mahmoud Fouad Elmorshedy, *Student Member, IEEE*, Yi Liu, *Member, IEEE*, Jose Rodriguez, *Fellow, IEEE*, and Cristian Garcia, *Member, IEEE*

***Abstract*—One of the methods that is used to increase the efficiency of the linear induction machine (LIM) is the maximum thrust per ampere (MTPA), where the same thrust can be achieved with a lower value of the primary current. Consequently, the power loss can be decreased and the efficiency be increased. However, so far, no quantitative focus exists to increase the efficiency of the LIM. This article proposes the MTPA-based finite-set model predictive control. The concept of field-oriented control is used to achieve the condition of MTPA. Based on this condition, the proposed control method can be developed by adjusting the value of the primary flux linkage. The proposed control method depends on both thrust and primary flux linkage and this proposed method is called finite-set model predictive direct thrust control (FS-MPDTC). Comparison between the FS-MPDTCs with and without MTPA is presented to illustrate the effectiveness of the proposed method. A prototype test platform is developed in the laboratory with two 3 kW arc induction machines to verify the proposed method. Analysis for both comprehensive simulation and experimental results are conducted in this article.**

***Index Terms*—Finite-set model predictive control (FS-MPC), finite-set model predictive direct thrust control (FS-MPDTC), linear induction machine (LIM), maximum thrust per ampere (MTPA).**

Manuscript received May 13, 2019; revised September 29, 2019; accepted December 4, 2019. Date of publication December 14, 2019; date of current version March 13, 2020. This work was supported in part by the National Natural Science Foundation of China under Grants 51877093 and 51707079, in part by the National Key Research and Development Program of China under Grant YS2018YFGH000299, in part by the Key Technical Innovation Program of Hubei Province under Grant 2019AAA026, and in part by the Fundamental Research Funds for the Central Universities under Grant 2019kfyXMBZ031. Recommended for publication by Associate Editor R. Kennel. *(Corresponding author: Yi Liu.)*

W. Xu and Y. Liu are with the State Key Laboratory of Advanced Electromagnetic Engineering and Technology School of Electrical and Electronic Engineering, Huazhong University of Science and Technology, Wuhan 430074, China (e-mail: weixu@hust.edu.cn; liuyi82@hust.edu.cn).

M. F. Elmorshedy is with the State Key Laboratory of Advanced Electromagnetic Engineering and Technology, School of Electrical and Electronic Engineering, Huazhong University of Science and Technology, Wuhan 430074, China and also with the Department of Electrical Power and Machines Engineering, Faculty of Engineering, Tanta University, Tanta 31527, Egypt (e-mail: mahmoud.elmorshedy@f-eng.tanta.edu.eg).

J. Rodriguez is with the Universidad Andres Bello, Santiago 7550196, Chile (e-mail: jose.rodriguez@unab.cl).

C. Garcia is with the Universidad de Talca, Curico 3340000, Chile (e-mail: cristian.garcia@utalca.cl).

Color versions of one or more of the figures in this article are available online at http://ieeexplore.ieee.org.

Digital Object Identifier 10.1109/TPEL.2019.2960280

I. Introduction

In 1960s, linear electric machines have been developed and attracted to the industry applications [1]. Linear induction machines (LIMs) have been paid great attention from both academia and industry due to their merits of direct linear motion, strong acceleration or deceleration, low maintenance cost, small cross area, small turning circus, and so on [2]–[6].

Till now, there have been more than 20 commercial metro lines based on linear machines all over the world, including Kennedy Airline in America, both of Trans-Rapid Line used in Beijing Airport and Line 4 used in Guangzhou Subway in China, and so on [1], [7].

Although the LIMs are with various merits, they have some demerits such as end effect and higher air gap, which degrade the dynamic performance [8]. This effect results from the special structure of the LIM where the cut-open magnetic circuit of the primary with an entry end and an exit end makes the air-gap flux attenuated, because the induced entry end eddy currents can significantly cause the variation of mutual inductance and additional nonlinearities [9]. These demerits make the control characteristics of LIMs more complicated than those of rotating induction machines (RIMs). Moreover, the influence of the end effect is neglected by the classical control strategies for LIMs, which result in imperfect drive performance.

Both of direct thrust control (DTC) [10]–[12] and field-oriented control (FOC) [13]–[16] are developed to obtain better performance for LIMs. However, some demerits are inevitable with both of DTC and FOC. An improved method has been proposed in [17] to overcome these problems and demerits associated with the classical DTC, by which the lower primary flux linkage and thrust ripples (TRs) can be achieved but the fixed switching frequency cannot be achieved. However, this achievement in [17] is not sufficient and extra improvements should be done to enhance the drive characteristics of LIMs.

Unlike the offline switching table that used in DTC, recently, the model predictive control (MPC) can be used to select more effective input voltage vectors by online evaluation. The MPC is regarded as the most reliable approach for online optimization with multivariable control, low current distortion, and reduced switching losses [18]. The MPC can be categorized as continuous control set and finite control set [19]. The DTC can be combined with the finite-set model predictive control, and

known as model predictive torque control (MPTC) for RIMs [20]. Hence, for conventional RIMs, the finite-set model predictive direct torque control with different strategies has been used as an alternative solution for the DTC because of the discrete nature and limited number of states of the two-level three-phase voltage source inverter (VSI) [21]. For the LIMs, the finite-set model predictive DTC (FS-MPDTC) has been developed in the authors' previous work [22].

The principle of FS-MPDTC is to pick out the best switching vector that can minimize the cost function, which can be then applied in the next control period [23]. The cost function used for FS-MPDTC consists of the absolute thrust and primary flux linkage errors. Nowadays, the performance of FS-MPTC can be further improved by modifying and enhancing the cost function or using a proper modulation strategy [24]–[26]. Some of these modifications are done by adding some criteria in the cost function. Although, these modifications have been developed to enhance the performance of the drive system but it would increase the computational burden. In addition, the complexity and sensitivity to any error in the prediction process would be increased, which may lead to wrong selection of switching vectors. Besides, the performance of the controller looks like that of the FOC technique. In [24], the cost function is designed to achieve the maximum thrust per ampere (MTPA), but it contains four weighting factors that need to be tuned. It is difficult to obtain the satisfactory weights for this cost function, because it has been demonstrated that the weighting factors are difficult to be selected when the cost function has more than two weighting factors [20]. On the other hand, the control technique based on the concept of discrete duty-cycle has been presented in [26] to decrease the stator flux linkage and torque ripples for the RIMs. Instead of using the torque ripple minimization or deadbeat method to calculate the exact period of the active voltage vector, a fixed period has been used. In addition, the maximum torque per ampere is not presented.

In order to obtain the high performance and increase the efficiency of the electric drive system, the MTPA can be used. For conventional RIM, a new cost function has been proposed with only one weighting factor in [25] instead of four weighting factors that have been presented in [24]. However, in [25], the stator flux is not controlled and thus high ripples of the stator flux are still generated.

For LIMs, an indirect FOC-based optimum slip is developed in [27] to increase the thrust with the same primary current. This method suffers from many offline calculations and tests to obtain the optimum slip, which can be stored in the switching table for online operation.

Despite comprehensive research for conventional rotating machines presented in [18]–[22], few works have focused on FS-MPDTC for LIM applications. Also, to the best knowledge of the authors, the MTPA based on FS-MPDTC strategy is not well investigated for the LIM applications.

Therefore, this article proposes an MTPA method based on FS-MPDTC for LIMs to reduce the primary current for the same thrust load, increase the efficiency, and reduce the TRs. The concept of FOC is used to achieve the condition of MTPA. Then, the FS-MPDTC is improved to achieve MTPA without adding more weighting factors. To confirm the effectiveness and capability of the MTPA-based FS-MPDTC method, a comparison between FS-MPDTCs with and without MTPA is presented and discussed in this article. Moreover, the end effect is taken into consideration for all of dynamic models of the LIM, MTPA condition, and FS-MPDTC strategy. Finally, both simulation and experimental results prove the capability of the proposed method for achieving the same thrust with minimum current.

II. Dynamic Model of LIM and Steps for Obtaining Condition of MTPA

Great attentions from the researchers are oriented to develop the exact dynamic model for LIMs due to the end effect [28]. The value of $f(Q)$ can be used to represent the end effect as described by

$$f(Q) = (1 - \exp(-Q))/Q \tag{1}$$

where its value depends on end-effect factor Q as given by

$$Q = D_s R_2 / [v_2 (L_{l2} + L_m)] \tag{2}$$

where v_2 is the machine speed, and D_s is the primary length.

Therefore, the amplitude of f(Q) is utilized to modify the magnetizing inductance as

$$L_{\text{meq}} = [1 - f(Q)] L_m \tag{3}$$

where the standstill value of mutual inductance is L_m [3].

To fulfill the maximum thrust per ampere (MTPA), the FOC strategy is used. Therefore, the synchronous reference frame for LIM dynamic model is required. The primary and secondary voltage equation in dq-axis can be written as

$$u_{dq1} = R_1 i_{dq1} + p\psi_{dq1} - j\omega_1 \psi_{dq1} \tag{4}$$

$$u_{dq2} = R_2 i_{dq2} + p\psi_{dq2} - j(\omega_1 - \omega_2)\psi_{dq2}. \tag{5}$$

The primary and secondary flux linkage equations in the *dq*-axis can be deduced as

$$\psi_{dq1} = L_1 i_{dq1} + L_{\text{meq}} i_{dq2} \tag{6}$$

$$\psi_{dq2} = L_2 i_{dq2} + L_{\text{meq}} i_{dq1} \tag{7}$$

where the u_{dq1} and u_{dq2} are the *dq*-axis of primary and secondary voltage respectively; R_1 and R_2 are the primary and secondary resistance, respectively; ψ_{dq1} and ψ_{dq1} are the *dq*-axis of primary and secondary flux linkage, respectively; and L_1 and L_2 are the primary and the secondary self-inductances, respectively.

Depending on the principle of FOC technique, all amplitude of secondary flux linkage of LIM is oriented only in the direction of the d-axis where $\psi_{d2} = \psi_2$ while there is no secondary flux linkage is remaining in the direction of *q*-axis $\psi_{q2} = 0$, as shown in Fig. 1. Consequently, in steady-state operations of the LIM, both of the primary and the secondary currents in *dq*-axis can be derived from (5), (6) and Fig. 1 as follows:

$$i_{d2} = 0 \tag{8}$$

$$i_{q2} = -\frac{L_{\text{meq}}}{L_2} i_{q1} \tag{9}$$

$$i_{d1} = I_1 \cos(\theta) \tag{10}$$

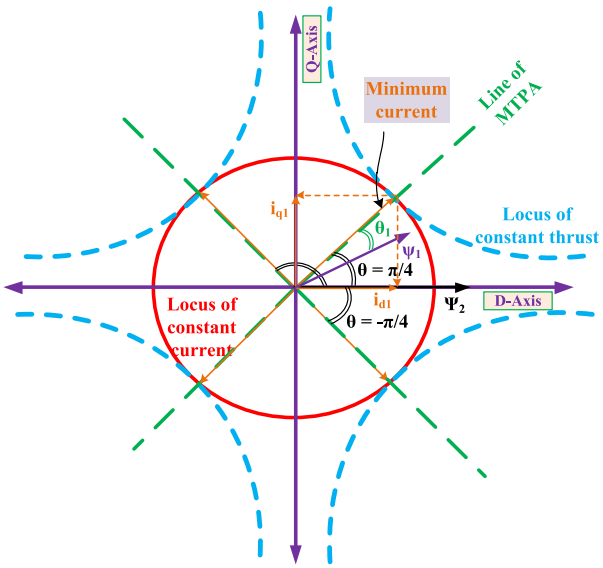

Fig. 1. Primary current in dq-axis and different angles of θ with both of primary and secondary flux linkage vectors in dq-axis.

$$i_{q1} = I_1 \sin(\theta) \tag{11}$$

where θ is the angle between the primary current vector and d-axis.

Moreover, the secondary flux linkage and the developed thrust can be calculated in the steady-state from the following forms:

$$|\psi_2| = \psi_{d2} = L_{\text{meq}} i_{d1} \tag{12}$$

$$F_e = \frac{3}{2}\frac{\pi}{\tau}\frac{L_{\text{meq}}^2}{L_2} i_{d1} i_{q1}. \tag{13}$$

For a limitation on the primary current, the value of both d- and q-axis primary currents of LIM should not be increased more than their maximums, as expressed by

$$i_{d1}^2 + i_{q1}^2 \le I_{\max}^2 \tag{14}$$

where $I_{\max}$ is the maximum allowable primary current.

Based on the developed thrust (13), the locus of the primary current is hyperbolical when the thrust is constant, while from (14), the locus is a circle, as in Fig. 1.

As the orientation of the secondary flux linkage in the direction of d-axis, the value of d-axis primary current should only be a positive value. On the other hand, the value of primary current in q-axis may be positive or negative value based on the second derivation of the thrust.

Thus, the value of angle θ has two values ($\pi/4$ and $-\pi/4$), where the same thrust can be obtained with the minimum magnitude of primary current as noticed from Fig. 1.

Consequently, the amplitude of d-axis and q-axis current is equal ($i_{d1} = i_{q1}$) because the angle is $\pi/4$, where the same thrust can be achieved with minimum current at this angle.

In the steady-state operation of the LIM, the dq-axis of primary flux linkage can be obtained based on the principle of FOC

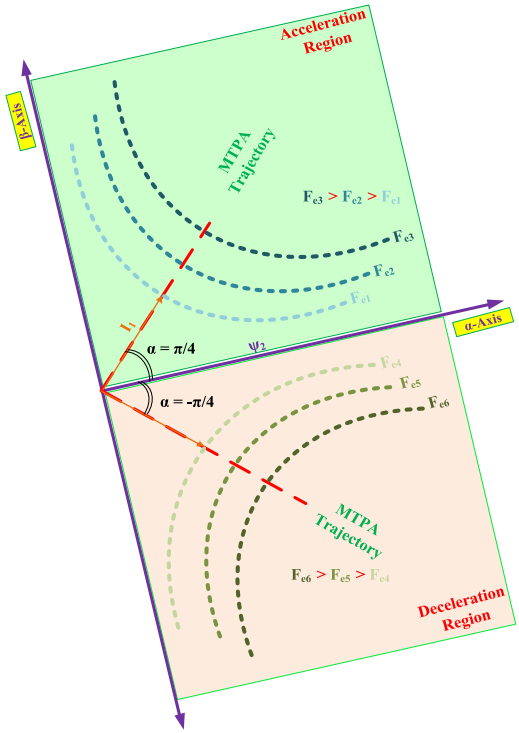

Fig. 2. Acceleration and deceleration regions of LIM according to α in $\alpha\beta$-axis with the relation between the trajectory of primary current and constant thrust.

technique and the condition of MTPA as follows:

$$\left.\begin{aligned} \psi_{d1} &= L_1 i_{d1} \\ \psi_{q1} &= L_1 i_{q1} - \frac{L_{\text{meq}}^2}{L_2} i_{q1} = (L_1 - \frac{L_{\text{meq}}^2}{L_2}) i_{d1} \end{aligned}\right\} \tag{15}$$

$$\psi_1 = \sqrt{\psi_{d1}^2 - \psi_{q1}^2} = \sqrt{L_1^2 - (L_1 - \frac{L_{\text{meq}}^2}{L_2})^2}\, i_{d1} = KK i_{d1} \tag{16}$$

where $KK = \sqrt{L_1^2 - (L_1 - \frac{L_{\text{meq}}^2}{L_2})^2}$.

In addition, the developed thrust can be obtained under the condition of MTPA ($i_{d1} = i_{q1}$) by

$$F_e = K i_{d1}^2 \tag{17}$$

where $K = \frac{3}{2}\frac{\pi}{\tau}\frac{L_{\text{meq}}^2}{L_2}$.

From (16) and (17), the relationship between the developed thrust and the primary flux linkage can be obtained. Hence, the reference primary flux linkage can be calculated from the reference thrust, as described by

$$\psi_1^* = KK * \sqrt{F_e^*/K}. \tag{18}$$

The same analysis and derivation can be obtained when $\alpha\beta$-axis is used instead of dq-axis, as illustrated in Fig. 2, where in stationary reference frame the angle θ is replaced with angle α.

III. Proposed MTPA-Based FS-MPDTC for LIM

FS-MPDTC can be used to obtain lower thrust and primary flux linkage ripples compared to conventional control strategies

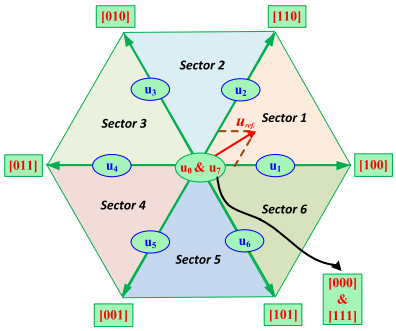

Fig. 3. Eight voltages vectors for the two-level VSI.

with the help of using two or three voltage vector in one sample period, but these lead to much complication and more calculation process [29]. In addition, the switching frequency of the FS-MPDTC is variable and not constant like in the other control strategies [29], and the usage of the variable switching frequency can reduce the torque ripples [30]–[32]. Therefore, only one voltage vector is used in the proposed cost function and improved by the penalty function for safe operation. In addition, the value of the reference primary flux linkage is adjusted according to the previous analysis in Section II to achieving MTPA. Moreover, the linear speed of LIM is control based on FS-MPDTC where PI controller is employed to regulate the linear speed to track the reference value. The PI controller generates the reference thrust and the reference primary flux linkage is developed from the reference thrust. The principles of FS-MPDTC are based mainly on three steps. First, the estimation step, second the prediction step, and finally, the cost function. In general, the estimated and the predicted variable depend on the selected and the designed cost function. For FS-MPDTC, the designed cost function contains both of primary flux linkage and thrust errors that should be minimized. Hence, the variables that are used for the first step and second step are as follows: first, primary and secondary flux linkage estimation, and second, prediction for primary flux linkage, primary current and developed thrust. The objective of the designed and the selected cost function is to determine the optimum switching vector for the used power converter which minimizes this cost function. For two-level VSI, all of the eight voltage vectors are used in the prediction stage to select the optimum one. The arrangement and the switching state for each voltage vector are shown in Fig. 3. In the following, the equations that are used for FS-MPDTC algorithm:

1) Secondary and primary flux linkage estimation in $\alpha\beta$-axis: The secondary and primary flux linkage can be estimated depending on the principles of flux observer in [33] considering the mathematical model of LIM as following:

$$\vec{\psi}_2(k) = \frac{R_2 T_s L_{\text{meq}} \vec{i}_1(k)}{[L_2 + R_2 T]} - \frac{jT_s L_2 \omega_2 \vec{\psi}_2(k) + L_2 \vec{\psi}_2(k-1)}{[L_2 + R_2 T]} \tag{19}$$

$$\vec{\psi}_1(k) = \frac{\vec{\psi}_2(k)}{\tau_l} + \sigma \vec{i}_1. \tag{20}$$

2) Primary flux linkage, primary current, and the developed thrust prediction in $\alpha\beta$-axis for the next period: Time discretization for the continuous model of LIM based on first-order Euler method is used for predicting the primary flux linkage $\psi_1(k+1)$, the primary current $i_1(k+1)$ and thrust $F_e(k+1)$ for the next instant. The following equations are deduced to predict the next-instant for all of them as:

$$\vec{\psi}_{1,i}(k+1) = \vec{\psi}_1(k) + T_s \vec{u}_{1,i}(k) - T_s R_1 \vec{i}_1(k) \tag{21}$$

$$\vec{i}_{1,i}(k+1) = \left[-\frac{T_s}{\sigma}\left(R_1 + \frac{R_2}{\tau_l^2}\right) + 1\right]\vec{i}_1(k) + \frac{T_s}{\sigma}\left(\vec{u}_{1,i}(k) + \left(\frac{1}{\tau_r \tau_l} - j\frac{\omega_2}{\tau_l}\right)\vec{\psi}_2(k)\right) \tag{22}$$

$$F_{e,i}(k+1) = \frac{3}{2}\frac{\pi}{\tau}\text{Im}\left(\vec{\psi}^*_{1,i}(k+1) \otimes \vec{i}_{1,i}(k+1)\right) \tag{23}$$

where $\sigma = (L_1 - \frac{L_{\text{meq}}^2}{L_2})$,$\tau_r = \frac{L_2}{R_2}$, $\tau_l = \frac{L_2}{L_{\text{meq}}}$,$u_{1,i}(k)$ is one of the eight voltage vectors [u_1(0, 1, 2, …,7)] shown in Fig. 3, and T_s is the sampling period.

3) Cost function design: The main purpose of the FS-MPDTC is to keep the required value of developed thrust and primary flux linkage around its reference value with minimum ripples for both of them. The appropriate selection for the control action can be considered as one of the voltage vectors [u_1(0, 1, 2, …,7)] which leads to the system variables $F_e(k+1)$ and $\psi_1(k+1)$ tracks the desired reference value F_{eref} and $\psi_{1\text{ref}}$.

As previously mentioned, the designed cost function based on the absolute errors between the predicted system variables and the reference values for both thrust and primary flux linkage. Moreover, in order to ensure the safe operation without overcurrent during the start-up and dynamic operation, it is necessary to introduce the current limit into the proposed FS-MPDTC by adding an overcurrent penalty function term *I* in the cost function. Therefore, the cost function g can be expressed as

$$g = |F_{\text{eref}} - F_{ei}(k+1)| + C\,|\psi_{1\text{ref}} - \psi_{1i}(k+1)| + I \tag{24}$$

where *C* represents the weighting factor, and it is important because of different units between the two terms of cost function. Equation (25) can be used to determine the starting tuning value of the weighting factor [34], as illustrated by

$$C = F_r / |\psi_r| \tag{25}$$

where F_r is the rated thrust value, and $|\psi_r|$ the rated amplitude of primary flux linkage.

On the other hand, the value of the overcurrent penalty function term *I* can be determined by

$$I = \begin{cases} \infty & \text{if } \sqrt{i_{\alpha 1}^2(k+1) + i_{\beta 1}^2(k+1)} > I_{\max} \\ 0, & \text{otherwise} \end{cases} \tag{26}$$

where $I_{\max}$ is the maximum permitted current.

Moreover, more additional computing cost will be brought as a result of the time delay compensation. Hence, the time of execution for FS-MPDTC will be increased with heavy computational burden. In addition, it is difficult to obtain the

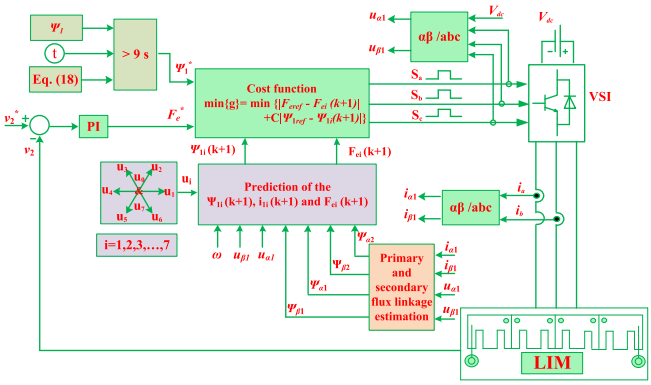

Fig. 4. Complete schematic diagram for the proposed MTPA-based FS-MPDTC with adjustable speed drive for LIM.

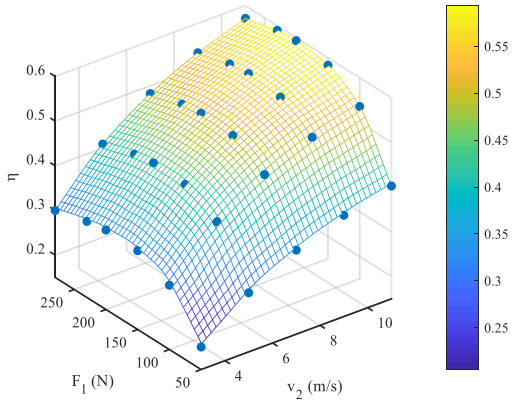

Fig. 5. Efficiency of LIM based on FS-MPDTC without MTPA.

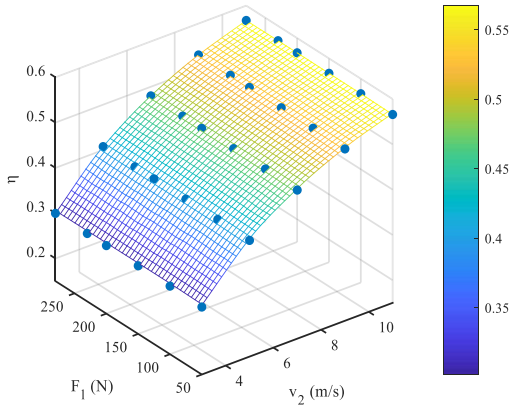

Fig. 6. Efficiency of LIM based on FS-MPDAC with MTPA.

TABLE I
LIM PARAMETERS

Parameter	Symbol	Value	Unit
Secondary resistance	R_2	2.4	Ω
Secondary leakage inductance	L_{l2}	0.0043	H
Primary resistance	R_1	1	Ω
Primary length	D_s	1.3087	m
Pole pitch	τ	0.1485	m
Rated power	P_r	3	kW
Rated thrust	F_r	280	N
Rated current	I_r	22	A
Rated speed	V_r	11	m/s

TABLE II
CONTROL PARAMETERS

Quantity	Symbol	Value
Weighting factor	C	704.5
Proportional gain	K_p	2000
Integral gain	K_i	6.34

exact and the correct parameters of LIM under the effects of both end-effect and edge effect so that one more prediction for delay compensation will increase the errors of prediction [35]. Consequently, in this article, the proposed control strategy is presented without the delay compensation method in [36].

The complete schematic diagram for the proposed MTPA based on FS-MPDTC with adjustable speed drive is shown in Fig. 4.

IV. SIMULATION AND EXPERIMENTAL RESULTS

To check the capability and the effectiveness of the proposed control strategy of MTPA-based FS-MPDTC, the proposed method is compared without and with MTPA. The proposed method is evaluated using MATLAB/Simulink model while the experimental results are investigated based on prototype test platform of arc induction machine (AIM). The AIM prototype parameters are the same in both simulation and experiments. All data related to AIM machine that are used in the tests of the simulation are listed in Table I. While the initial value of weighting factor is calculated according to (25), the used value and the gains of the used PI controller are given in Table II.

In general, the LIM suffer from low efficiency because of the large air-gap length. Moreover, the end-effects lead to a parameter changes where the magnetizing inductance decreases with the increase of speed and resulting in more additional losses and therefore deterioration of drive efficiency. Therefore, the estimated efficiency at the rated condition of the employed LIM is about 55%.

Without and with MTPA the efficiency of the machine is tested based on FS-MPDTC control strategy for different levels of speed and load, as shown in Figs. 5 and 6, respectively. From these two figures in terms of efficiency, it can be concluded that when the machine operates at light-load conditions the efficiency is low while, the efficiency becomes higher when the load or speed increases. While, for the same load and speed, the efficiency of LIM with MTPA based FS-MPDTC is higher than FS-MPDTC without MTPA because the phase current of the LIM under the FS-MPDTC without MTPA is much higher.

A. Simulation Studies and Results

To illustrate the effectiveness of FS-MPDTC over the DTC with space vector modulation technique (DTC-SVM) and FOC, first the steady-state performance comparisons are presented. After that, the MTPA-based FS-MPDTC strategy is used to

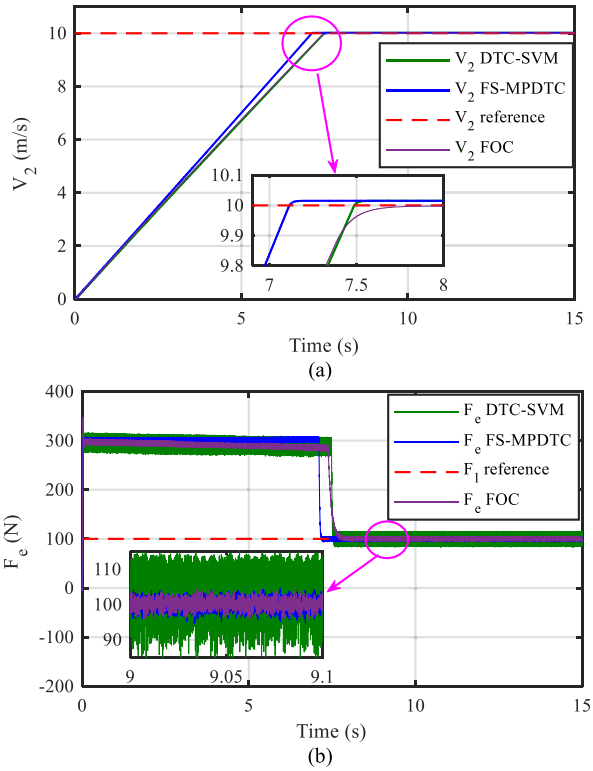

Fig. 7. Comparison between DTC-SVM, FOC and FS-MPDTC methods for LIM. (a) Speed. (b) Thrust.

test the overall system performance under both speed and load variations.

1) Steady State Performance Comparison: The FS-MPDTC without MTPA is compared with other standard DTC-SVM strategy and FOC strategy to illustrate the advantages and disadvantages between all of them. The comparison has been done at the same sample frequency ($Ts = 1 * 10^{-5}$), the same reference speed ($v_2 = 10$ m/s), and the same thrust load ($F_L = 100$ N). Fig. 7(a) and (b) illustrates the steady-state comparison between all control methods. It can be noticed that the actual speed of LIM reaches quickly its reference value when FS-MPDTC is used compared to other control techniques. The FOC with fixed switching frequency is based on using three voltage vectors in one sampling period that gives the chance to achieve lower TR. Regarding the FS-MPDTC, it is categorized as variable switching frequency [29]. According to the operation of the variable switching frequency of FS-MPDTC, the lower TR can be obtained [30], [32]. The percentage of such ripples can be got as the same level of FOC, which would be reduced to a lower one if two voltage vectors are used in the switching period [37].

In addition, the percentages of TR for all the control methods are summarized in Table III based on the following equation:

$$F_{\text{ripple}}\% = \frac{\Delta F_{e-pp}}{F_L} * 100 \tag{27}$$

where $\Delta F_{e-\text{pp}}$ is the half value between peak to peak of the developed TR value.

2) Variable Thrust Load and Constant Reference Speed: In this case, the FS-MPDTC with and without MTPA is tested under different thrust loads where the thrust load change from 100 and 200 N, respectively while the reference speed is kept at 8 m/s. To illustrate the advantage of FS-MPDTC with MTPA over and FS-MPDTC without MTPA, the first 9 s is used for starting and without the MTPA and after 9 s the MTPA strategy is applied with different thrust loads. It can be noticed from Fig. 8(a) that the control strategy succeeded in keeping the measured speed follows the reference speed under the different values of thrust loads. The developed thrust is varied around the load thrust as shown in Fig. 8(b). While the primary flux linkage well tracks the reference value with and without MTPA based FS-MPDTC, as shown in Fig. 8(c). In addition, the three-phase instantaneous primary current and the rms value for phase-A without and with MTPA is shown in Fig. 8(d) and (e), respectively. From these two figures it can be observed that under the same thrust load the primary current is reduced when the MTPA control strategy is activated. In the case of MTPA, the reference value of the primary flux linkage is calculated from the reference thrust and hence it contains variation and oscillation, which makes the THD of the primary current much higher than that without MTPA. These harmonics causes eddy current and hysteresis losses but with two or three voltage vectors in one sampling period these harmonics can be reduced. Otherwise, the variation of the difference angle between the secondary flux linkage angle and the primary current angle is illustrated in Fig. 8(f). It can be noticed that the difference angle is kept around 45° with the proposed MTPA.

TABLE III
COMPARISON OF THE TR AMONG DTC-SVM, FOC AND FS-MPDTC

Quantity	DTC-SVM	FOC	FS-MPDTC
TR%	$F_{ripple}\% = \frac{15}{100} * 100 = 15\%$	$F_{ripple}\% = \frac{5}{100} * 100 = 5\%$	$F_{ripple}\% = \frac{7}{100} * 100 = 7\%$

3) Constant Thrust Load and Variable Reference Speed: In this subsection, the proposed control technique is studied under different levels of speed to validate the capability of the proposed control strategy. The reference speed is increased to 10 m/s from 7 m/s after 14 s from starting, as shown in Fig. 9(a). It can be observed from this figure that the measured speed follows the reference speed during all step changes in the speed. The developed and load thrust during speed variation is shown in Fig. 9(b), where the proposed strategy is activated at 9 s. On the other hand, the FS-MPDTC can develop lower primary flux linkage ripples as shown in Fig. 9(c).

Both instantaneous and rms primary current for phase-A without and with MTPA is illustrated in Fig. 9(d) and (e). As shown, the lower primary current can be obtained by using the proposed MTPA control strategy. Moreover, the difference angle is maintained constant at 45° when the proposed MTPA based on the FS-MPDTC is activated at 9 s under speed variation, as shown in Fig. 9(f).

4) FS-MPDTC With and Without MTPA Under Rated Speed: In this case, the FS-MPDTC is studied for both with MTPA and

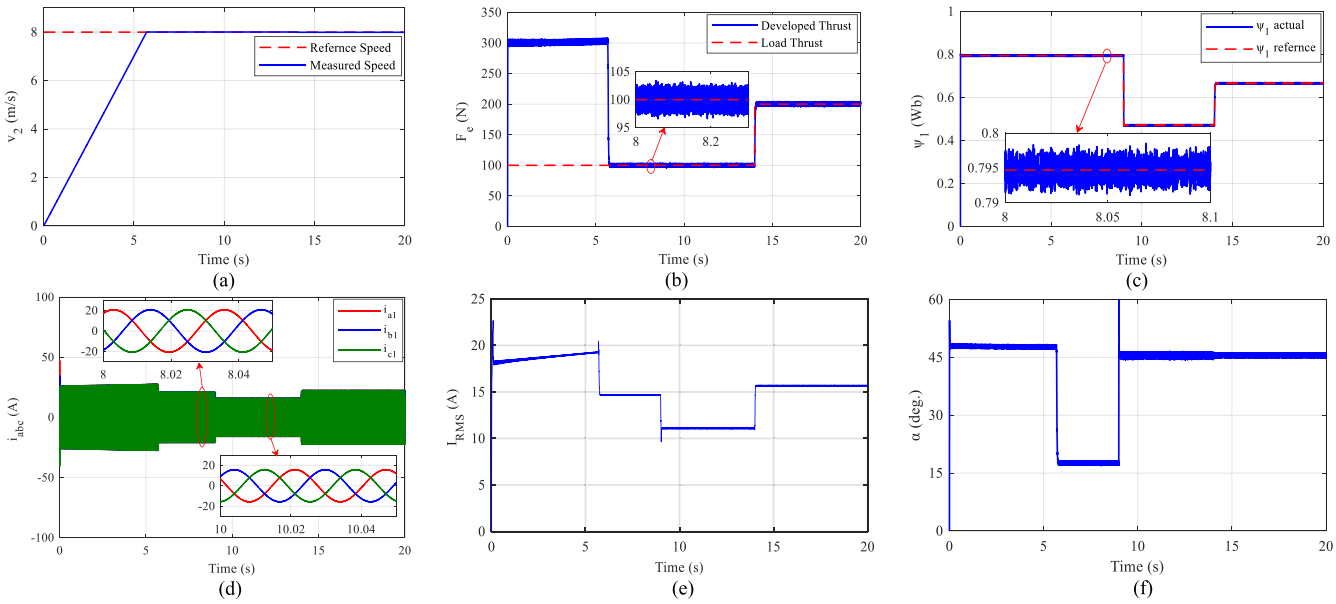

Fig. 8. MTPA-based FS-MPDTC for variable thrust load and constant speed. (a) Speed. (b) Thrust. (c) Primary flux. (d) Three-phase instantaneous primary current. (e) Phase-A primary current rms value. (f) Difference angle.

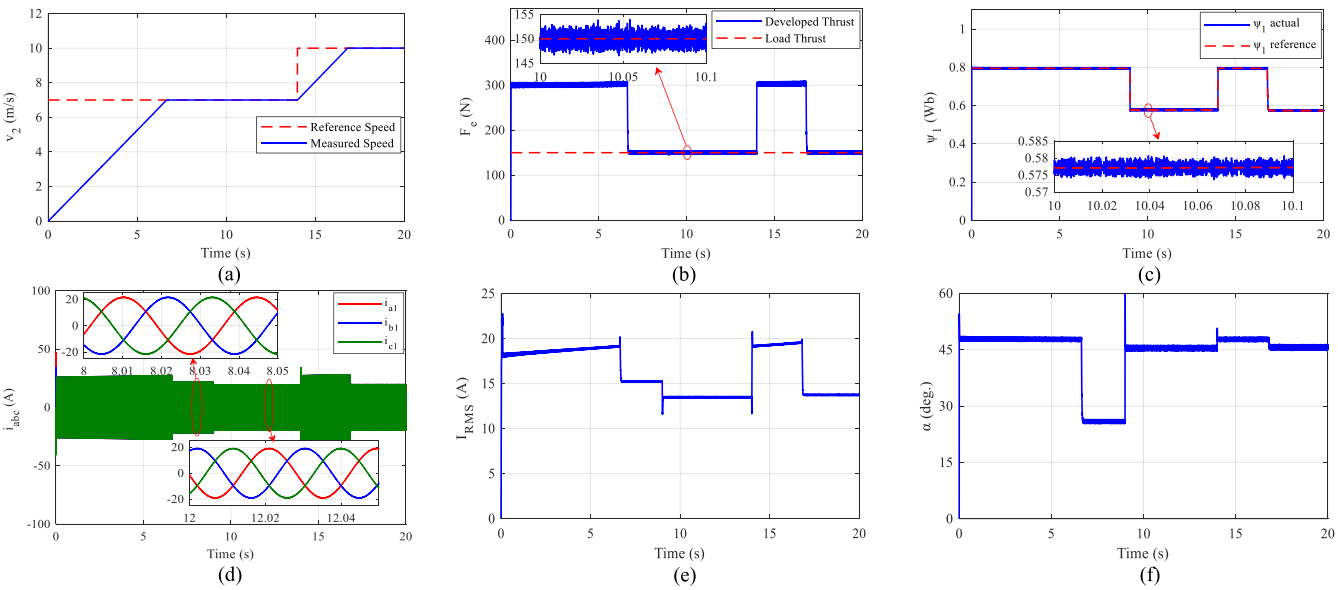

Fig. 9. MTPA-based FS-MPDTC for variable speed and constant thrust load. (a) Speed. (b) Thrust. (c) Primary flux. (d) Three-phase instantaneous primary current. (e) Phase-A primary current rms value. (f) Difference angle.

without MTPA where the reference speed is rated value (11 m/s) and the thrust load changes from 80 to 140 N. Fig. 10 shows the effect of FS-MPDTC without MTPA under the rated speed. On the other hand, the effect of FS-MPDTC with MTPA is presented in Fig. 11. Moreover, the comparison of FS-MPDTC with and without MTPA on the same figure is presented in Fig. 12 to illustrate the benefit of MTPA over that without MTPA. It can be noticed from Fig. 12(b) that the primary current with MTPA is always less than the primary current without MTPA during the steady-state operation. While during the dynamic state, the primary current can be kept almost the same by the help of limitation.

5) Parameter Uncertainty: The estimation method that is used for the prediction of the secondary flux linkage and the primary current is based on the mathematical model of the machine which depends on and calculated from the machine parameters. Therefore, the sources of any error in the estimated values come from the parameters mismatch, such as primary resistance, secondary resistance and mutual inductance. Therefore, the parameter sensitivity analysis of the optimal flux calculation,

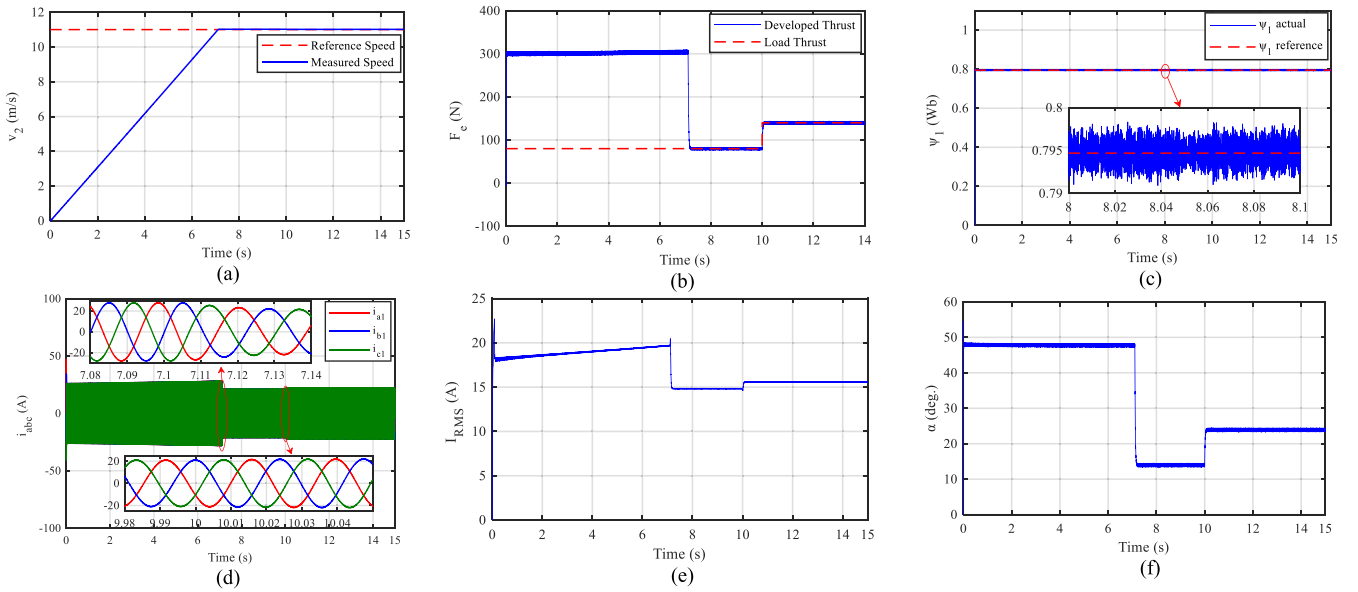

Fig. 10. FS-MPDTC without MTPA under the rated speed and load change. (a) Speed. (b) Primary flux linkage. (c) RMS primary current. (d) Thrust. (e) Angle. (f) Instantaneous three phase current.

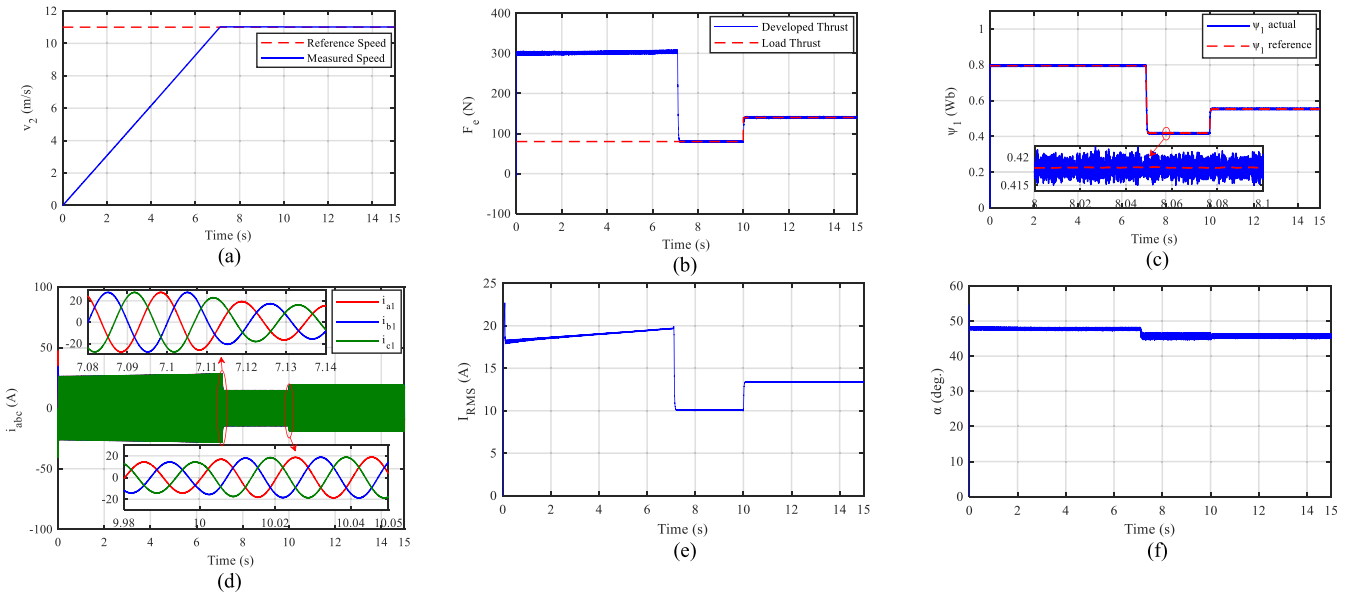

Fig. 11. FS-MPDTC with MTPA under the rated speed and load change. (a) Speed. (b) Primary flux linkage. (c) RMS primary current. (d) Thrust. (e) Angle. (f) Instantaneous three phase current.

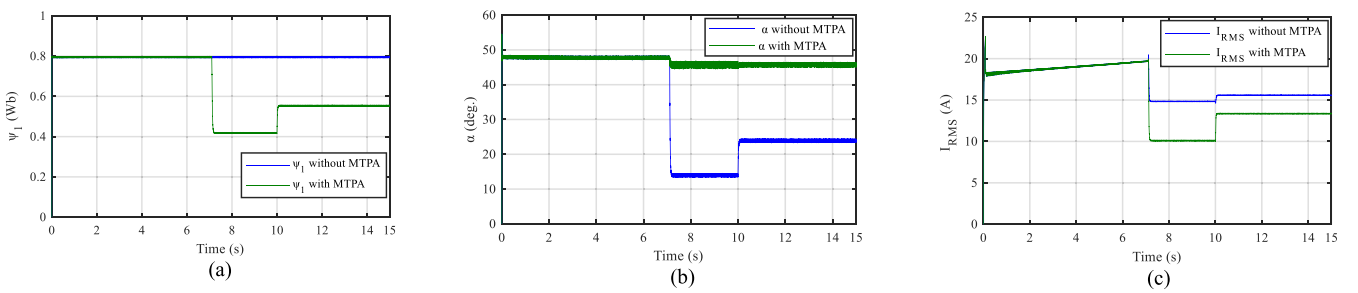

Fig. 12. Comparison for FS-MPDTC with and without MTPA. (a) Primary flux linkage. (b) Angle. (c) RMS primary current.

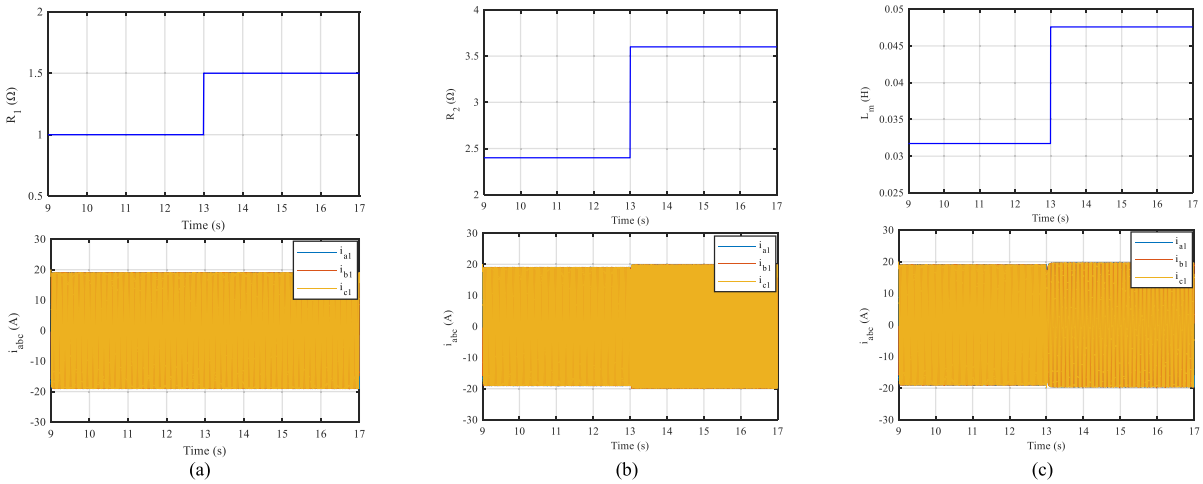

Fig. 13. Impact of the parameters mismatch on the proposed FS-MPDTC. (a) Mismatch of the primary resistance. (b) Mismatch of the secondary resistance. (c) Mismatch of the mutual inductance.

based on the optimal value of the primary flux linkage equation, is studied to check the impact of the errors on the accuracy of the proposed control strategy.

a) Mismatch in Primary and Secondary Resistances: The optimal primary flux linkage, aided with (18), can be written without simplification in the following form:

$$\psi_1^* = \sqrt{L_1^2 - \left(L_1 - \frac{L_{\text{meq}}^2}{L_2}\right)^2} * \sqrt{\frac{2\tau L_2 F_e^*}{3\pi L_{\text{meq}}^2}}. \tag{28}$$

It can be noticed that the primary and secondary resistances have not been included in (28). Hence, the optimal flux linkage will not change with the mismatch in these two quantities.

b) Mutual Inductance Mismatch: On the other side, the mutual inductance has been included in the optimal flux linkage relation. Thus, this can lead to an impact on the performance. First of all, the mutual inductance can be expressed by (29), to include the effect of its mismatch, as illustrated by

$$L_{\text{meq}} = L'_{\text{meq}} + \Delta L_{\text{meq}} \tag{29}$$

where L'_{meq} denotes the original value, and $\Delta L'_{\text{meq}}$ represents its associated mismatch.

For its very small value in this work, the secondary leakage inductance can be neglected. Hence, the secondary inductance equals the mutual inductance, as described by

$$L_2 = L_{\text{meq}}. \tag{30}$$

Substituting both (29) and (30) into (28), the optimal value of the primary flux linkage can be written as

$$\psi_1^* = \sqrt{L_{1l}^2 + 2L_{1l}L_{\text{meq}} + L_{\text{meq}}^2 - L_{1l}^2} * \sqrt{\frac{2\tau F_e^*}{3\pi L_{\text{meq}}}} \tag{31}$$

$$\psi_1^* = \sqrt{2L_{1l} + L_{\text{meq}}} * \sqrt{\frac{2\tau F_e^*}{3\pi}} \tag{32}$$

$$\psi_1^* = \sqrt{2L_{1l} + L'_{\text{meq}} + \Delta L_{\text{meq}}} * \sqrt{\frac{2\tau F_e^*}{3\pi}}. \tag{33}$$

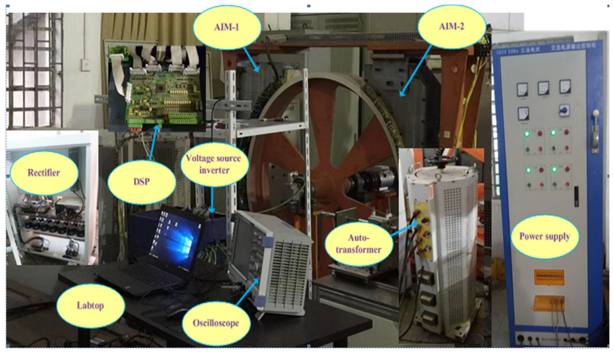

Fig. 14. Photograph of the experimental setup.

Aided with (33), it can be noticed that the mismatch of mutual inductance has a small effect because of the root square.

From the view point of the high accuracy confirmation of the proposed control strategy on the whole system performance, a case study is selected under parameter mismatch where the reference thrust is set as 100 N at 6 m/s. The primary resistance R_1, the mutual inductance L_m, and the secondary resistance R_2 are increased to 1.5 times of its original value and this increase is much high and not practical. The effects of these mismatches are illustrated in Fig. 13.

It can be observed from Fig. 13 that the uncertainty and mismatch of the primary resistance has no impact on the primary current. However, the mismatches of both mutual inductance and the secondary resistance have a small effect on the primary current. Therefore, the proposed method is slightly sensitive to secondary resistance mismatch and mutual inductance, but considers robust corresponding to the primary resistance mismatch.

B. Experimental Results

A test bench of 3 kW AIM is used to evaluate the effectiveness of the MTPA based FS-MPDTC strategy, as shown in Fig. 14. The air gap of LIM used in the metro application is about 10 mm thus the design of the test bench AIM is based on the large

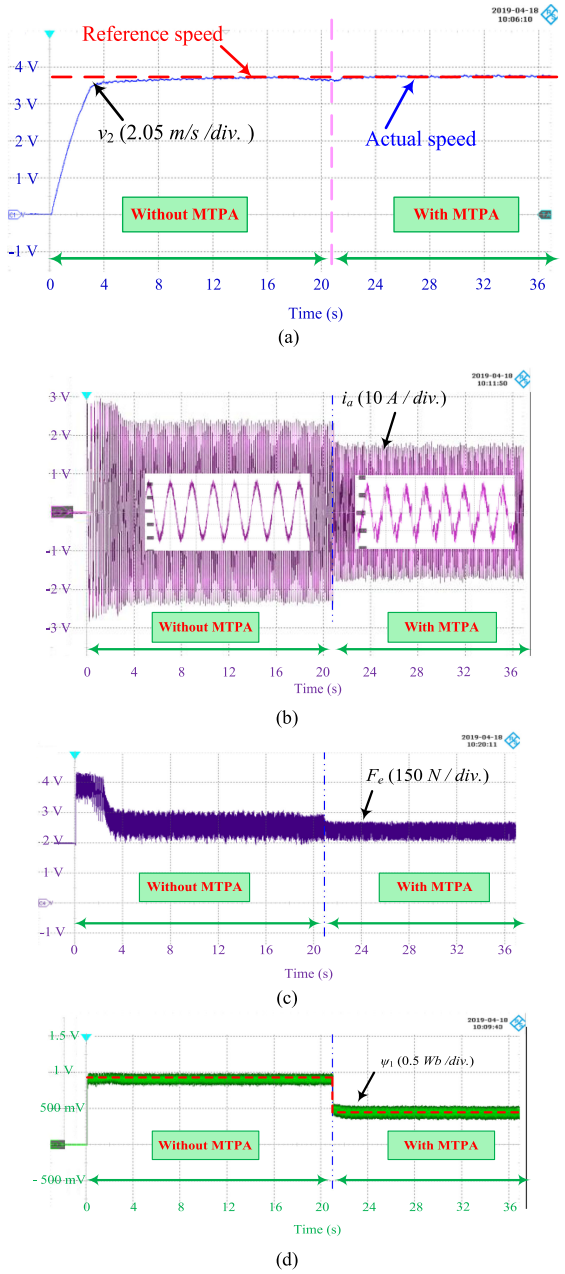

Fig. 15. Experimental validation of FS-MPDTCs with and without MTPA. (a) Linear speed. (b) Primary phase-A current. (c) Developed thrust. (d) Primary flux linkage.

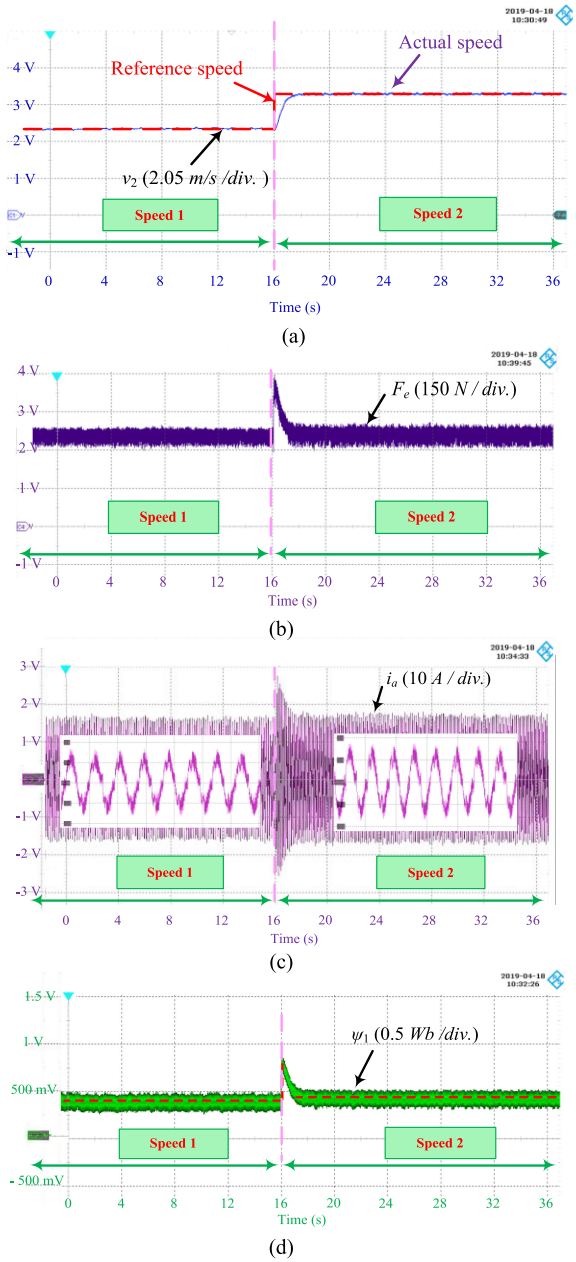

Fig. 16. Experimental verification of MTPA-based FS-MPDTC under different levels of linear speed. (a) Linear speed. (b) Developed thrust. (c) Primary phase-A current. (d) Primary flux linkage.

diameter of the rotor reaches to 1.25 m to emulate the actual metro. The characteristics of the AIM with this design are much similar to the LIM [38] and hence the same steps of the proposed control method can be applied to the AIM instead of LIM. In addition, the used test bench contains two AIM one on the right side and other on the left side and each one is 3 kW, as shown in Fig. 14. The right AIM is used for testing the proposed control method while the left AIM is used as a mechanical load. Both of them are controlled by digital signal processor (DSP) board (TMS320F28335) and supplied by three-phase two-level VSI. The rotating speed is measured by using an incremental encoder while the primary current is measured through Hall current sensor. On the other hand, the three-phase primary voltage is calculated by measuring the value of dc-link voltage and knowing the switching states of the applied voltage vector.

The used switching and sampling frequency are 10 kHz. As the secondary leakage inductance is small value, it can be eliminated from the prediction equations to simplify the DSP code. The effectiveness of the proposed MTPA based FS-MPDTC is evaluated under different conditions.

1) Constant Speed With and Without MTPA-Based FS-MPDTC: To validate the advantages of using MTPA-based FS-MPDTC a comparison of FS-MPDTC with and without MTPA is presented and studied in this case. First, the AIM

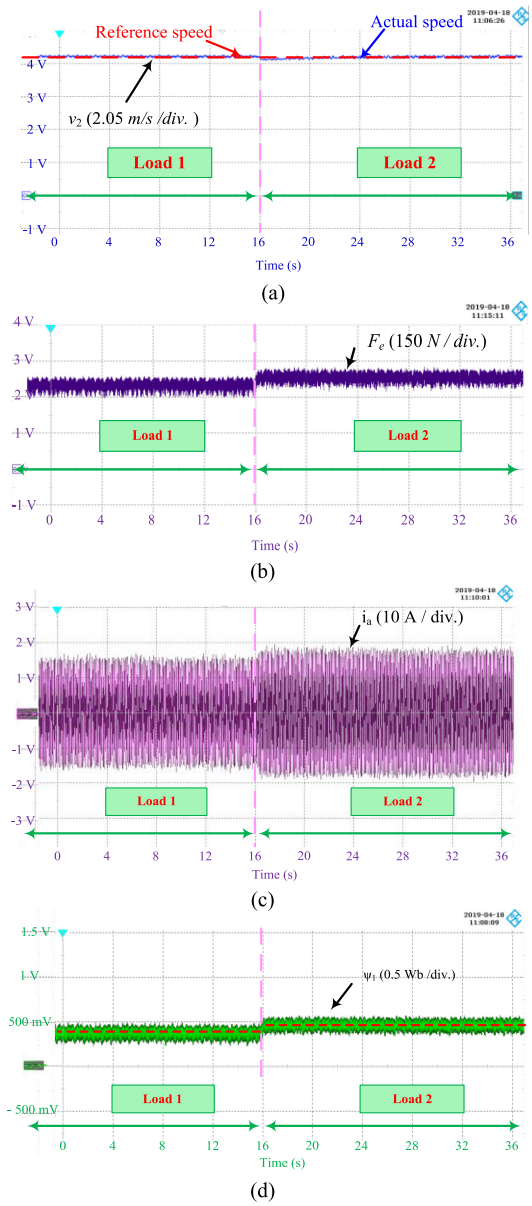

Fig. 17. Experimental confirmation of MTPA-based FS-MPDTC under different levels of thrust load. (a) Linear speed. (b) Developed thrust. (c) Primary phase-A current. (d) Primary flux linkage.

is controlled by FS-MPDTC without MTPA for approximately 20 s then MTPA is activated. In this case, the primary voltage is the same value for both FS-MPDTC with and without MTPA. The linear speed is kept constant at the required reference value 7.5 m/s as shown in Fig. 15(a). The primary phase-A current is illustrated in Fig. 15(b). It can be noticed that the primary current is reduced by 20% when the MTPA is activated. In addition, the developed thrust is remained constant at the required load 50 N with small ripples compared to the same control method without considering MTPA, as shown in Fig. 15(c). Moreover, the primary flux linkage is regulated around the reference value, as illustrated in Fig. 15(d).

2) Variable Speed With MTPA-Based FS-MPDTC: In this case, the proposed MTPA-based FS-MPDTC is applied under linear speed profile of two different levels where the first level of speed is 5 m/s and then the speed is increased to 7 m/s, as shown in Fig. 16(a) while the thrust load is constant. The developed thrust is maintained constant at the required load thrust 50 N as noticed from Fig. 16(b). The corresponding primary current to the thrust load is illustrated in Fig. 16(c). While the primary flux linkage tracks the reference value under different linear speed, as observed from Fig. 16(d).

3) Variable Thrust Load With MTPA-Based FS-MPDTC: For more validation from the proposed MTPA, the control performance is tested under different thrust loads and the linear speed kept constant at 9 m/s. The control strategy succeeded in returning the linear speed to the reference value after the thrust load is increased, as shown in Fig. 17(a). Fig. 17(b) shows the developed thrust load where the load is increased from 50 N to approximately 100 N. Moreover, the corresponding primary current to the thrust load variation is illustrated in Fig. 17(c). The reference value of the primary flux linkage is related to the reference developed load thrust hence when the load thrust is increased, the reference primary flux linkage is increased and the control strategy is kept the actual value around the reference value to achieve the MTPA, as observed from Fig. 17(d).

V. Conclusion

In general, the LIM suffers from low efficiency because of the large air-gap length. In order to address this issue, this article proposes a strategy with the combination of MTPA and FS-MPDTC for LIM drive systems. The proposed MTPA-based FS-MPDTC strategy is successful in minimizing the primary current for the same thrust. Meanwhile, lower TR and higher efficiency can be obtained because the primary current and copper losses are reduced effectively. Finally, the proposed strategy is carried out in an AIM prototype of 3 kW. By comprehensive simulation and experimental validation, it is obvious that the proposed strategy can reduce the primary current at different speeds and loads in comparison with the FS-MPDTC without MTPA.

References

[1] I. Boldea, L. Tutelea, W. Xu, and M. Pucci, "Linear electric machines, drives and MAGLEVs: An overview," *IEEE Trans. Ind. Electron.*, vol. 65, no. 9, pp. 7504–7515, Sep. 2018.

[2] D. Hu, W. Xu, R. Dian, Y. Liu, and J. Zhu, "Loss minimization control of linear induction motor drive for linear metros," *IEEE Trans. Ind. Electron.*, vol. 65, no. 9, pp. 6870–6880, Sep. 2018.

[3] W. Xu, R. Dian, Y. Liu, D. Hu, and J. Zhu, "Robust flux estimation method for linear induction motors based on improved extended State observers," *IEEE Trans. Power Electron.*, vol. 34, no. 5, pp. 4628–4640, May 2019.

[4] F. Alonge, M. Cirrincione, F. Drippolito, M. Pucci, and A. Sferlazza, "Active disturbance rejection control of linear induction motor," *IEEE Trans. Ind. Appl.*, vol. 53, no. 5, pp. 4460–4471, Sep./Oct. 2017.

[5] I. Boldea, *Linear Electric Machines, Drives, and MAGLEVs Handbook*. Boca Raton, FL, USA: CRC Press, 2013.

[6] J. Zou, W. Xu, X. Yu, Y. Liu, and C. Ye, "Multistep model predictive control with current and voltage constraints for linear induction machine based urban transportation," *IEEE Trans. Veh. Technol.*, vol. 66, no. 12, pp. 10817–10829, Dec. 2017.

[7] W. Xu, J. G. Zhu, and Y. Zhang, "Equivalent circuits for single-sided linear induction motors," *IEEE Trans. Ind. Appl.*, vol. 46, no. 6, pp. 2410–2423, Nov./Dec. 2010.

[8] H. Karimi, S. Vaez-zadeh, and F. R. Salmasi, "Combined vector and direct thrust control of linear induction motors with end effect compensation," *IEEE Trans. Energy Convers.*, vol. 31, no. 1, pp. 196–205, Mar. 2016.

[9] F. Alonge, M. Cirrincione, M. Pucci, and A. Sferlazza, "Input-output feedback linearization control with on-line MRAS-based inductor resistance estimation of linear induction motors including the dynamic end effects," *IEEE Trans. Ind. Appl.*, vol. 52, no. 1, pp. 254–266, Jan./Feb. 2016.
[10] M. Cheema, J. E. Fletcher, M. Farshadnia, and M. F. Rahman, "Sliding mode based combined speed and direct thrust force control of linear permanent magnet synchronous motors with first-order plus integral sliding condition," *IEEE Trans. Power Electron.*, vol. 34, no. 3, pp. 2526–2538, Mar. 2019.
[11] M. Cheema, J. E. Fletcher, M. Farshadnia, D. Xiao, and M. F. Rahman, "Combined speed and direct thrust force control of linear permanent-magnet synchronous motors with sensorless speed estimation using a sliding-mode control with integral action," *IEEE Trans. Ind. Electron.*, vol. 64, no. 5, pp. 3489–3501, May 2017.
[12] M. Cheema, J. E. Fletcher, D. Xiao, and M. F. Rahman, "A linear quadratic regulator-based optimal direct thrust force control of linear permanent-magnet synchronous motor," *IEEE Trans. Ind. Electron.*, vol. 63, no. 5, pp. 2722–2733, May 2016.
[13] D. Hu, W. Xu, R. Dian, and Y. Liu, "Loss minimization control strategy for linear induction machine in urban transit considering normal force," *IEEE Trans. Ind. Appl.*, vol. 55, no. 2, pp. 1536–1549, Mar. 2019.
[14] A. Accetta, M. Cirrincione, M. Pucci, and G. Vitale, "Closed-loop MRAS speed observer for linear induction motor drives," *IEEE Trans. Ind. Appl.*, vol. 51, no. 3, pp. 2279–2290, May/Jun. 2015.
[15] A. Accetta, M. Cirrincione, and M. Pucci, "Neural sensorless control of linear induction motors by a full-order luenberger observer considering the end effects," *IEEE Trans. Ind. Appl.*, vol. 50, no. 3, pp. 1891–1904, May/Jun. 2014.
[16] P. Marino, M. Milano, and F. Vasca, "Linear quadratic state feedback and robust neural network estimator for field-oriented-controlled induction motors," *IEEE Trans. Ind. Electron.*, vol. 46, no. 1, pp. 150–161, Feb. 1999.
[17] Q. G. Ke Wang, Y. Li, and L. Shi, "A novel switching scheme for direct thrust control of LIM with reduction of thrust ripple," in *Proc. Int. Con. Elect. Mach. Syst.*, 2010, pp. 1491–1494.
[18] M. Amiri, J. Milimonfared, and D. A. Khaburi, "Predictive torque control implementation for induction motors based on discrete space vector modulation," *IEEE Trans. Ind. Electron.*, vol. 65, no. 9, pp. 6881–6889, Sep. 2018.
[19] P. Cortes, M. P. Kazmierkowski, R. M. Kennel, D. E. Quevedo, and J. Rodriguez, "Predictive control in power electronics and drives," *IEEE Trans. Ind. Electron.*, vol. 55, no. 12, pp. 4312–4324, Dec. 2008.
[20] M. Habibullah, D. D.-C. Lu, D. Xiao, and M. F. Rahman, "A simplified finite-state predictive direct torque control for induction motor drive," *IEEE Trans. Ind. Electron.*, vol. 63, no. 6, pp. 3964–3975, Jun. 2016.
[21] W. Xie *et al.*, "Finite-control-set model predictive torque control with a deadbeat solution for PMSM drives," *IEEE Trans. Ind. Electron.*, vol. 62, no. 9, pp. 5402–5410, Sep. 2015.
[22] M. F. Elmorshedy, W. Xu, and Y. Liu, "Speed control of linear induction motor with thrust and stator flux ripple reduction," in *Proc. Int. Con. Elect. Mach. Syst.*, 2018, pp. 1789–1794
[23] M. Mamdouh and M. A. Abido, "Efficient predictive torque control for induction motor drive," *IEEE Trans. Ind. Electron.*, vol. 66, no. 9, pp. 6757–6767, Sep. 2019.
[24] M. Preindl and S. Bolognani, "Model predictive direct torque control with finite control set for PMSM drive systems, part 1: Maximum torque per ampere operation," *IEEE Trans. Ind. Inform.*, vol. 9, no. 4, pp. 1912–1921, Nov. 2013.
[25] S. A. Davari, "Predictive direct angle control of induction motor," *IEEE Trans. Ind. Electron.*, vol. 63, no. 8, pp. 5276–5284, Aug. 2016.
[26] M. R. Nikzad, B. Asaei, and S. O. Ahmadi, "Discrete duty-cycle-control method for direct torque control of induction motor drives with model predictive solution," *IEEE Trans. Power Electron.*, vol. 33, no. 3, pp. 2317–2329, Mar. 2018.
[27] K. Wang, Y. Li, Q. Ge, and L. Shi, "An improved indirect field-oriented control scheme for linear induction motor traction rives," *IEEE Trans. Ind. Electron*, vol. 65, no. 12, pp. 9928–9937, Dec. 2018.
[28] W. Xu *et al.*, "Equivalent circuits for single-sided linear induction motors," *IEEE Trans. Ind. Appl.*, vol. 46, no. 6, pp. 2410–2423, Nov./Dec. 2010.
[29] Y. Zhang, B. Xia, H. Yang, and J. Rodriguez, "Overview of model predictive control for induction motor drives," *Chin. J. Elect. Eng.*, vol. 2, no. 1, pp. 62–76, Jun. 2016.
[30] D. Jiang, Q. Li, X. Han, and R. Qu, "Variable switching frequency PWM for torque ripple control of AC motors," in *Proc. Int. Con. Elect. Mach. Syst.*, Chiba, Japan, 2016, pp. 1–5.
[31] P. Karamanakos, P. Stolze, R. M. Kennel, S. Manias, and H. du Toit Mouton, "Variable switching point predictive torque control of induction machines," *IEEE J. Emerg. Sel. Topics Power Electron.*, vol. 2, no. 2, pp. 285–295, Jun. 2014.
[32] D. Jiang and F. Wang, "Current-ripple prediction for three-phase PWM converters," *IEEE Trans. Ind. Appl.*, vol. 50, no. 1, pp. 531–538, Jan./Feb. 2014.
[33] P. L. Jansen and R. D. Lorenz, "A physically insightful approach to the design and accuracy assessment of flux observers for field-oriented induction machine drives," *IEEE Trans. Ind. Appl.*, vol. 30, no. 1, pp. 101–110, Jan./Feb. 1994.
[34] Y. Zhang and H. Yang, "Model predictive torque control of induction motor drives with optimal duty cycle control," *IEEE Trans. Power Electron.*, vol. 29, no. 12, pp. 6593–6603, Dec. 2014.
[35] X. Zhang, L. Zhang, and L Zhang "Model predictive current control for PMSM drives with parameter robustness improvement," *IEEE Trans. Power Electron.*, vol. 34, no. 2, pp. 1645–1657, Feb. 2019.
[36] P. Cortes, J. Rodriguez, C. Silva, and A. Flores, "Delay compensation in model predictive current control of a three-phase inverter," *IEEE Trans. Ind. Electron.*, vol. 59, no. 2, pp. 1323–1325, Feb. 2012.
[37] J. Zou, W. Xu, J. Zhu, and Y. Liu, "Low-complexity finite control set model predictive control with current limit for linear induction machines," *IEEE Trans. Ind. Electron.*, vol. 65, no. 12, pp. 9243–9254, Dec. 2018.
[38] A. Majumdar and T. K. Bhattacharya, "Comparison of force developed in a linear induction machine and an equivalent arc linear induction machine at zero velocity," in *Proc. IEEE Int. Con. Power Electron., Drives Energy Syst.*, Chennai, India, 2018, pp. 1–5.

Wei Xu (Senior Member, IEEE) received the double B.E. and M.E. degrees from Tianjin University, Tianjin, China, in 2002 and 2005, and the Ph.D. degree from the Institute of Electrical Engineering, Chinese Academy of Sciences, Beijing, China, in 2008, all in electrical engineering.

From 2008 to 2012, he was a Postdoctoral Fellow with the University of Technology Sydney, Sydney, Australia, the Vice Chancellor Research Fellow with the Royal Melbourne Institute of Technology, Melbourne, Australia, and the Japan Science Promotion Society Invitation Fellow with Meiji University, Tokyo, Japan. Since 2013, he has been a Full Professor with the State Key Laboratory of Advanced Electromagnetic Engineering and Technology, Huazhong University of Science and Technology, Wuhan, China. His research interests include design and control of linear/rotary machines.

Dr. Xu is a Fellow of the Institute of Engineering and Technology (IET). He has served as Associate Editor for several Journals, such as IEEE TRANSACTIONS ON INDUSTRIAL ELECTRONICS, and so on.

Mahmoud Fouad Elmorshedy (Student Member, IEEE) was born in Gharbeya, Egypt in 1989. He received the B.Sc. and M.Sc. degrees in electrical engineering from Tanta University, Tanta, Egypt, in 2012 and 2016, respectively. He is currently working toward the Ph.D. degree with the State Key Laboratory of Advanced Electromagnetic Engineering and Technology, Huazhong University of Science and Technology, Wuhan, China.

Since 2013, he worked as a Teaching Assistant with the Department of Electrical Power and Machines Engineering, Faculty of Engineering, Tanta University, where he was promoted to the post of Assistant Lecturer in June 2016. His current research interests include linear induction motor, predictive control, power electronics and renewable energy.

Yi Liu (Member, IEEE) received the B.E. and M.E. degrees in automation and control engineering from the Wuhan University of Science and Technology, Wuhan, China, in 2004 and 2007, respectively, and the Ph.D. degree in mechatronic engineering from the Huazhong University of Science and Technology, Wuhan, in 2016.

From 2007 to 2011, he was a Lecturer with the City College, Wuhan University of Science and Technology. From March 2016 to June 2016, he was a Senior R & D Engineer with the Fourth Academy of China Aerospace Science and Industry Group, Wuhan. In July 2016, he became a Postdoctoral Research Fellow with the State Key Laboratory of Advanced Electromagnetic Engineering and Technology, School of Electrical and Electronic Engineering, Huazhong University of Science and Technology. His current research interests include ac electrical machine control and inverter systems.

Jose Rodriguez (Fellow, IEEE) received the Engineer degree in electrical engineering from the Universidad Tecnica Federico Santa Maria, in Valparaiso, Chile, in 1977, and the Dr.-Ing. degree in electrical engineering from the University of Erlangen, Erlangen, Germany, in 1985.

Since 1977, he has been with the Department of Electronics Engineering, Universidad Tecnica Federico Santa Maria, as a Full Professor and President. Since 2015, he was the President, and since 2019, he is a Full Professor at Universidad Andres Bello in Santiago, Chile. He has authored and coauthored two books, several book chapters, and more than 400 journal and conference papers. His main research interests include multilevel inverters, new converter topologies, control of power converters, and adjustable-speed drives.

Dr. Rodriguez was the recipient of a number of best paper awards from journals of the IEEE. He is member of the Chilean Academy of Engineering. In 2014, he was the recipient the National Award of Applied Sciences and Technology from the Government of Chile and the Eugene Mittelmann Award from the Industrial Electronics Society of the IEEE in 2015. In years 2014–2019, he has been included in the list of Highly Cited Researchers published by the Web of Science.

Cristian Garcia (Member, IEEE) received the M.Sc. and Ph.D. degrees in electronics engineering from the Universidad Tecnica Federico Santa Maria (UTFSM), Valparaiso, Chile, in 2013 and 2017, respectively.

In 2016, he was a Visiting Ph.D. Student with the Power Electronics Machines and Control (PEMC) Group with the University of Nottingham, U.K. From 2017 to 2019, he was with the Engineering Faculty of the Universidad Andres Bello, Santiago, Chile, as an Assistant Professor. Since 2019, he has been with the Engineering Faculty, Universidad de Talca, Curico, Chile, where he is currently an Assistant Professor. His research interests include electric transportation applications, variable-speed drives, matrix converters, and model predictive control of power converters and drives.